Korean J. Chem. Eng., 37(6), 938-945 (2020)
DOI: 10.1007/s11814-020-0522-5

pISSN: 0256-1115
eISSN: 1975-7220

Defect-controlled Fe-N-doped carbon nanofiber by ball-milling for oxygen reduction reaction

**Yeonsun Sohn*, Dong-gun Kim*, Ji Ho Lee*, Sujin Lee*, In Seon Hwang*,
Soo-Hyoung Lee*, Sung Jong Yoo**,***,****, and Pil Kim*,†**

*School of Chemical Engineering, School of Semiconductor and Chemical Engineering, Solar Energy Research Center,
Jeonbuk National University, JeonJu, Jeonbuk 54896, Korea
**Fuel Cell Research Center, Korea Institute of Science and Technology, Seoul 02792, Korea
***Division of Energy & Environment Technology, KIST School, University of Science and Technology (UST),
Seoul 02792, Korea
****KHU-KIST Department of Converging Science and Technology, Kyung Hee University, Seoul 02447, Korea

(*Received 7 November 2019 • accepted 27 February 2020*)

Abstract−We demonstrate that control of the defect level on carbon materials is effective for enhancing the oxygen reduction reaction (ORR) performance of nonprecious-metal catalysts. Vapor-grown carbon nanofiber (VGCNF) with high crystallinity and high electronic conductivity was chosen as the substrate of our ORR catalysts. To induce defects on the VGCNF, it was subjected to ball-milling for various controlled times, yielding BM*x*-VGCNF (*x* represents the ball-milling time, 0-6 h). The defect level introduced on the VGCNF was effectively regulated by controlling the ball-milling time. Although the density of defect sites increased with increasing ball-milling time, the surface area was highest in BM2-VGCNF. Nonprecious-metal ORR catalysts (BM*x*-Fe-VGCNF) were prepared by NH_3 pyrolysis of Fe-ion-adsorbed BM*x*-VGCNF. The ball-milling of VGCNF was effective to introduce nitrogen onto the catalyst. In particular, the controlled ball-milling was important to generate highly active sites on the catalyst surface. Among the catalysts studied, BM2-Fe-VGCNF exhibited the best ORR performance, which was 2.5-times greater than that of BM*x*-Fe-VGCNF (*x*=4, 6).

Keywords: Fuel Cells, Oxygen Reduction Reaction (ORR), Non-precious Metal Catalysts, High-energy Ball-mill, Vapor Grown Carbon Nano Fiber (VGCNF)

INTRODUCTION

Polymer electrolyte membrane fuel cells (PEMFCs) are environmentally benign electrochemical devices with high energy conversion efficiency that can potentially be used as a power source for portable electronic devices and electric vehicles [1-3]. Despite the numerous advantages of PEMFCs over the conventional internal combustion engine, they are not widely used, in part because of their high manufacturing cost. In particular, the large amount of Pt-based catalyst used as the electrocatalyst for the oxygen reduction reaction (ORR) is one of the main factors impeding the broader application of PEMFCs [4-6].

To solve the aforementioned problem, researchers have devoted substantial effort to developing nonprecious-metal-based ORR catalysts with high activity and durability [7-11]. They include transition-metal oxides [12-14], transition-metal carbides [15,16], transition metals coordinated to nitrogen on carbon (*M*-N-C, where *M* represents the transition metal) [17-19], and carbons doped with heteroatoms [20,21]. Among them, *M*-N-C is promising in terms of catalytic performance, cost effectiveness, and natural abundance of the catalyst components.

The active sites of the *M*-N-C catalysts have been reported to be macrocyclic centers such as *M*-N*x* (*x* represents the number of nitrogen atoms), which are derived from a coordinated moiety of *M* and N [22-24]. Therefore, the content and electronic states are important factors determining the ORR performance. In particular, the coordination of *M* and N is essential for the manifestation of high ORR performance given the inferior ORR activity of nitrogen-containing carbon in the absence of a transition metal. The type of metal also influences the catalytic performance of *M*-N-C [25,26]. Among the metal elements, iron has been reported to be most active, showing four-electron selectivity when coordinated with pyridinic or pyrrolic nitrogen [27].

M-N-C catalysts have been prepared by pyrolyzing *M*-adsorbed carbon or *M*-adsorbed carbon precursors under various conditions. The doping of nitrogen can be achieved several ways, including through the use of nitrogen-containing carbon precursors [17,19], whereas NH_3 pyrolysis has frequently been used because it can be directly applied to conventional carbon supports [23-25]. Carbon is partly decomposed by the NH_3 pyrolysis process and simultaneously reacts with an iron precursor and NH_3, which produces a new structure such as *M*-N2-C and M-N4-C as a highly active site for ORR. The catalytic performance of *M*-N-C has been demonstrated to be dependent on the number of such accessible sites [27,28]. To

---

[†] To whom correspondence should be addressed.

E-mail: kimpil1@jbnu.ac.kr

increase the number of highly active sites, inducing a strong interaction between the catalyst components is important. However, the ORR performance of *M*-N-C is affected by the characteristics of the carbon substrate. The crystalline carbons with a sp^2 configuration are favored over amorphous carbons because crystalline carbons not only facilitate fast charge transfer in the catalyst layer but also resist oxidation, thereby improving the ORR performance [29-32]. Notably, highly active sites of *M*-N-C are generated on the walls of micropores of carbon when NH_3 is used as the nitrogen precursor. Thus, the introduction of nitrogen onto the carbon, corresponding to the formation of active sites, occurs through partial etching of the carbon during its reaction with NH_3. In this respect, the utilization of highly crystalline carbons might be a concern because the introduction of nitrogen is likely limited given their high oxidation resistance. Therefore, re-forming the surface of crystalline carbon so that nitrogen is easily incorporated into the carbon structure, forming highly active sites for the ORR, is critical.

In the present work, we chose vapor-grown carbon nanofibers (VGCNFs) as a carbon support because, in addition to their high electrical conductivity and strong resistance to oxidation, they can be produced on a large scale, further lowering the electrocatalyst cost when VGCNFs are incorporated into PEMFCs [33,34]. Notably, however, the surface of the VGCNF lacks functional groups, which makes anchoring metal ions and nitrogen groups difficult. We solved this problem by introducing defects onto the VGCNF surface. The defect sites generated on VGCNF likely serve as anchoring sites that support metal ions; more importantly, they also readily react with NH_3, enabling nitrogen to be easily introduced onto VGCNFs. We employed a high-energy ball mill to introduce defect sites onto the VGCNFs. The number of defect sites was controlled by varying the ball-milling time. Various characterizations were conducted to investigate the effect of ball-milling time on the characteristics of VGCNFs and VGCNF-derived *M*-N-C catalyst.

EXPERIMENTAL

1. Preparation of BM*x*-Fe-VGCNF Catalysts

VGCNFs (Carbon Nanomaterial Technology) were added to a ball-mill vial (Fritsch, TH-1080) with stainless balls. The mass ratio of ball and VGCNFs was 50 : 1. The ball-milling was conducted for 2, 4, or 6 h, and the samples were subsequently washed with concentrated HCl solution to remove residual metal species. The ball-milled samples are denoted as BM*x*-VGCNF (*x* represents the ball-milling time; *x*=0, 2, 4, 6). Adsorption of Fe ions onto BM*x*-VGCNF was by incipient wetness impregnation. The concentration of Fe ions on BM*x*-VGCNF was kept at 2 wt%. The Fe-ion-adsorbed BM*x*-VGCNF was pyrolyzed for 1 h at 900 °C under a mixed gas stream (50% N_2+50% NH_3) to yield the BM*x*-Fe-VGCNF catalysts.

2. Characterization and Electrochemical Measurements

Raman spectroscopy (Raman, Nanofinder 30) was used to study the configuration of carbon. The crystalline characteristics of the prepared samples were investigated by X-ray diffraction (XRD, Rigaku D/MAX 2500). The morphology of samples was monitored by transmission electron microscopy (TEM, JEOL 2010). The surface areas and pore volume were measured by N_2 physisorption (BELSORP-MINI (II)). The electronic state of nitrogen on the catalysts was examined by X-ray photoelectron spectroscopy (XPS, K-Alpha).

The electrochemical properties of the catalysts were investigated in an electrochemical cell composed of a reference electrode (Ag/AgCl (Cl saturated)), a counter electrode (Pt gauze), and a working electrode. The working electrode was prepared by coating a catalyst ink onto a rotating ring disk electrode (RRDE, PINE (AFE7R9GCPT)). The catalyst ink was prepared by dispersing a catalyst in a mixed solution of isopropyl alcohol (SAMCHUN), water, and Nafion ionomer (Sigma-Aldrich). The sample loading on the RRDEs was 297 μg/cm^2. Cyclic voltammetry was conducted at a scan rate of 50 mV/s in the potential range from 0.1 to 1.3 V (vs. RHE) in N_2-purged 0.1 M $HClO_4$ solution. Linear sweep voltammetry was carried out to evaluate the ORR performance of the prepared catalysts. The polarization curves were obtained by linear sweep voltammetry, where the potential was swept at 5 mV/s from 1.0 to 0.1 V (vs. RHE) and the rotating speed of the electrode was 800 rpm. The electron transfer number and the fraction of peroxide formation was calculated using the following equation: $n=4NI_D/(NI_D+I_R)$, $\%H_2O_2=50(4-n)$, where I_D, I_R, and N represent the disk current, the ring current, and the collection efficiency (0.37), respectively. Accelerated durability test (ADT) was conducted at a scan rate of 200 mV/s in the potential range from 0.75 to 1.05 V (vs. RHE) for 10,000 cycles in O_2-purged 0.1 M $HClO_4$ solution. For the purpose of comparison, a commercial Pt/C (Premetek) was electrochemically characterized under the same condition as that applied for BM*x*-Fe-VGCNF catalysts.

RESULTS AND DISCUSSION

1. Physical Properties of BM*x*-Fe-VGCNF Catalysts

The effect of ball milling on the integrity of VGCNF was confirmed by Raman spectroscopy. As shown in Fig. 1, the spectra of all of the samples show two characteristic bands at 1,358 and 1,588 cm^{-1}, assigned to the D-band and G-band, respectively, which are related to the configuration of the carbon component. The D-band originates from sp^3 carbon, whereas the G-band arises from sp^2 carbon [35]. More specifically, these bands are related to the crystal-

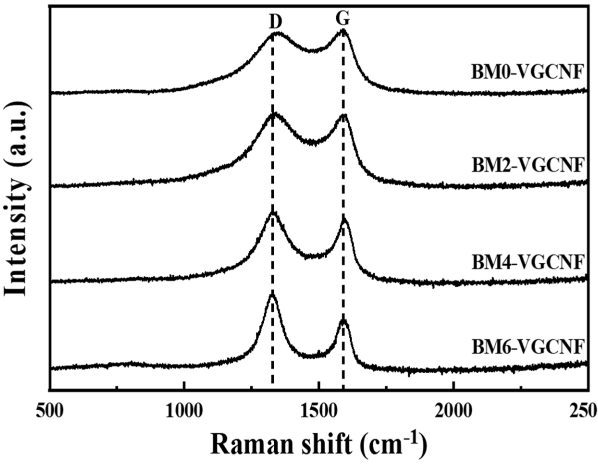

Fig. 1. Raman spectra of BM*x*-VGCNF samples.

Table 1. Summary of degree of defects, surface area and pore volume of BM*x*-VGCNF and BM*x*-Fe-VGCNF samples

	I_D/I_G[a]	Surface area (m^2g^{-1})	Pore volume (cm^3g^{-1})		Surface area (m^2g^{-1})	Pore volume (cm^3g^{-1})
BM0-VGCNF	0.9	156	0.03	BM0-Fe-VGCNF	139	0.02
BM2-VGCNF	0.98	345	0.08	BM2-Fe-VGCNF	809	0.22
BM4-VGCNF	1.08	293	0.07	BM4-Fe-VGCNF	463	0.1
BM6-VGCNF	1.30	275	0.06	BM6-Fe-VGCNF	438	0.09

[a] I_D and I_G represent the intensity of D-band and G-band in Raman spectra.

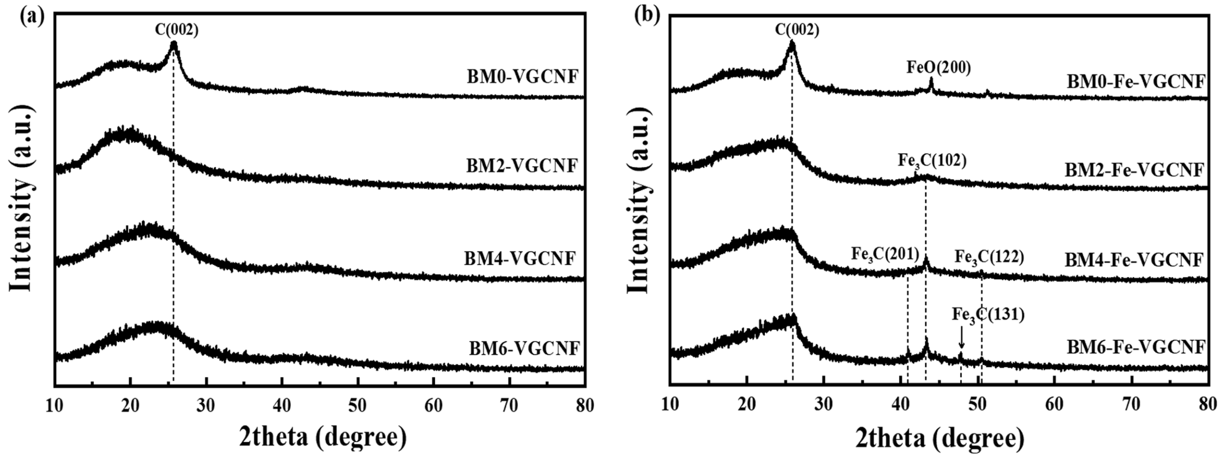

Fig. 2. XRD patterns of (a) BM*x*-VGCNF and (b) BM*x*-Fe-VGCNF.

linity of the carbon: the intensity of the G-band increases with increasing crystallinity of the carbon, and the intensity of the D-band increases with increasing concentration of carbon defect sites. We evaluated the degree of defects on our samples on the basis of the intensity ratio between the D-band and G-band (I_D/I_G). As listed in Table 1, this ratio increases with increasing ball-milling time, implying that ball-milling effectively introduces defect sites onto the VGCNF surface and, importantly, that the degree of defects can be controlled by changing the ball-milling time.

The crystallinity of BM*x*-VGCNF and BM*x*-Fe-VGCNF was confirmed by XRD. Among the BM*x*-VGCNF samples, as shown in Fig. 2(a), only BM0-VGCNF was observed to have generated peaks at 25.6°, which are assigned to the (002) planes of graphite, respectively [36]. These peaks disappeared in the patterns of the samples processed by ball-milling; however, the sp^2 carbon was not completely removed from these samples, as confirmed by their Raman spectra, which show a G-band. In addition to the characteristic peaks of graphite, additional peaks related to various iron species are observed in the XRD patterns of BM*x*-Fe-VGCNF. Interestingly, the generated iron species vary even though all of the catalysts were prepared under the same pyrolysis conditions. The peaks at 43.9° in the pattern of BM0-Fe-VGCNF are assigned to the (200) planes of FeO crystals, respectively [37]. On the contrary, the other catalysts derived from BM*x*-VGCNF (x=2, 4, 6) show peaks at 40.9, 43.2, 47.8, and 50.5, corresponding to the (201), (102), (131), and (122) planes of Fe_3C, respectively [37]. When Fe-ion-adsorbed carbon is pyrolyzed, as in the case of our BM*x*-Fe-VGCNF, iron oxides such as Fe_2O_3, Fe_3O_4, and FeO are usually formed on the catalysts. However, the formation of iron carbide, as observed on BM*x*-Fe-VGCNF (x=2, 4, 6), appears to be rare in the absence of a reactive carbon precursor. The carbon of defect sites generated by the ball-milling treatment is more reactive than sp^2 carbon; consequently, the formation of iron carbide is more predominant on BM*x*-Fe-VGCNF (x=2, 4, 6) than on BM0-Fe-VGCNF.

Fig. 3 shows TEM images of BM*x*-VGCNF and BM*x*-Fe-VGCNF. The BM0-VGCNF exhibits a long fiber-like morphology, whereas the ball-milled samples show small aggregated particles with various sizes. These results indicate that the fiber-like structure of VGCNF is broken down into small carbon pieces by the ball-milling process. The basic morphology of the BM*x*-Fe-VGCNF samples is similar to that of their counterpart BM*x*-VGCNF samples. Interestingly, BM0-Fe-VGCNF exhibits a fiber-like morphology similar to that of BM0-VGCNF even though it is prepared at a high temperature under an NH_3 stream. This similarity demonstrates that the structure of VGCNF itself is highly resistant to NH_3 etching at high temperatures; accordingly, the extent of nitrogen doping as well as the generation of pores is limited on BM0-VGCNF.

The surface area and pore volumes of BM*x*-VGCNF and BM*x*-Fe-VGCNF were measured on the basis of N_2 sorption; the results are summarized in Table 1. Compared with BM0-VGCNF, the ball-milled VGCNFs, BM*x*-VGCNF (x=2, 4, 6), have larger surface areas and larger pore volumes. Unlike BM0-VGCNF, as confirmed by TEM analysis, the BM*x*-VGCNF (x=2, 4, 6) samples contain a large number of small carbon particles generated by breaking the fiber-like structure of BM0-VGCNF. This observation implies that the new surface is produced during the ball-milling pro-

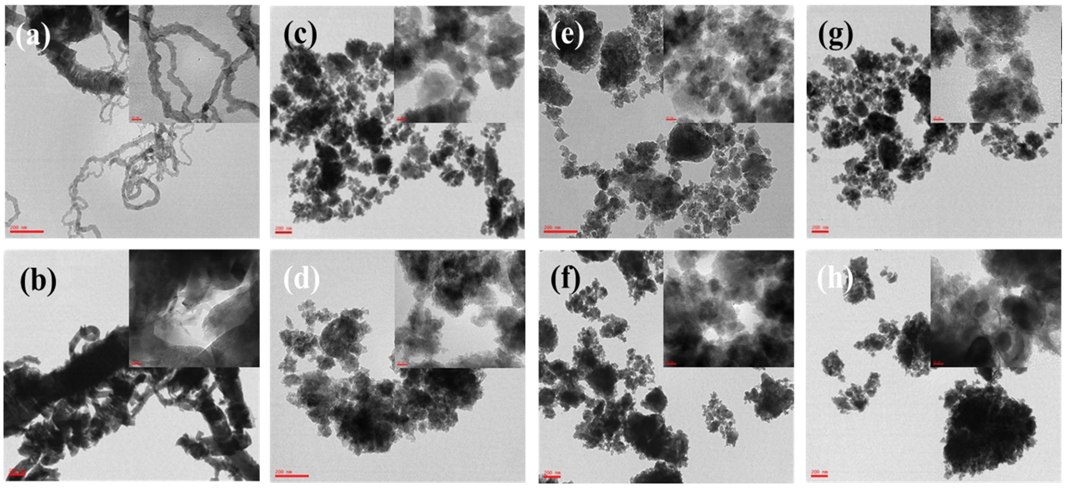

Fig. 3. TEM images of (a) BM0-VGCNF, (b) BM0-Fe-VGCNF, (c) BM2-VGCNF, (d) BM2-Fe-VGCNF (e) BM4-VGCNF, (f) BM4-Fe-VGCNF, (g) BM6-VGCNF, (h) BM6-Fe-VGCNF.

Table 2. Nitrogen content and XPS deconvolution result for N 1s spectra of BM*x*-Fe-VGCNF catalysts

	Nitrogen content (%)[a]	Species	Binding energy (eV)	Relative intensities (%)
BM0-Fe-VGCNF	0.9	Pyridinic N	398.1	34.7
		Pyrrolic N	400.3	42.9
		Quaternary N	401.3	22.4
BM2-Fe-VGCNF	2.1	Pyridinic N	398.4	66.0
		Pyrrolic N	400.8	25.2
		Quaternary N	402.4	8.8
BM4-Fe-VGCNF	2.4	Pyridinic N	398.4	60.1
		Pyrrolic N	400.8	27.6
		Quaternary N	402.4	12.3
BM6-Fe-VGCNF	2.8	Pyridinic N	398.4	50.3
		Pyrrolic N	400.8	36.1
		Quaternary N	402.3	13.6

[a]Measured by elementary analysis.

cess. Interestingly, the surface area and pore volume are highest in BM2-VGCNF and decrease with increasing ball-milling treatment, as observed in BM*x*-VGCNF (*x*=4, 6). The agglomeration of small carbon particles during the ball-milling treatment has been reported to be accompanied by the fracturing of large structures [35,38]. As the ball-milling time is extended, the agglomeration of small particles is likely to be dominant over the fracturing of large particles into small particles, leading to a decrease in surface area and pore volume, as observed for BM*x*-VGCNF (*x*=4, 6). Most of the prepared catalysts other than BM0-Fe-VGCNF were measured to have a higher surface area and greater pore volume than their BM*x*-VGCNF (*x*=2, 4, 6) counterpart. During pyrolysis, the carbon on the BM*x*-VGCNF reacts with NH_3 to produce a volatile product, resulting in the formation of pores in the samples [39]. In the case of BM*x*-VGCNF (*x*=2, 4, 6), the carbon in the defect sites is so reactive that a large number of pores are readily produced, resulting in enhanced surface area and pore volume. On the contrary, the surface area and pore volume of BM0-Fe-VGCNF are lower than that of BM0-VGCNF. Compared with BM*x*-VGCNF (*x*=2, 4, 6), BM0-VGCNF contains fewer defect sites. Therefore, the reaction with NH_3 is likely more limited than in the case of BM*x*-VGCNF (*x*=2, 4, 6), implying that pore generation is difficult. In addition, the formed iron oxide can block the pore mouth of BM0-Fe-VGCNF, leading to a decrease in the surface area and pore volume of BM0-Fe-VGCNF.

The nitrogen content of the catalysts was measured by elemental analysis. The nitrogen content of BM*x*-VGCNF was also measured but was negligible. As listed in Table 2, the nitrogen content increased with increasing ball-milling time. The introduction of nitrogen proceeds through the reaction between carbon and NH_3, and such reactions are facilitated when carbon resides on the defect sites. As confirmed by Raman spectroscopy, the defect sites become extensive with increasing ball-milling time; therefore, the nitrogen content also likely increases with increasing ball-milling time.

The electronic state of surface nitrogen on BM*x*-Fe-VGCNF was analyzed by XPS. As shown in Fig. 4, the spectra of all the sam-

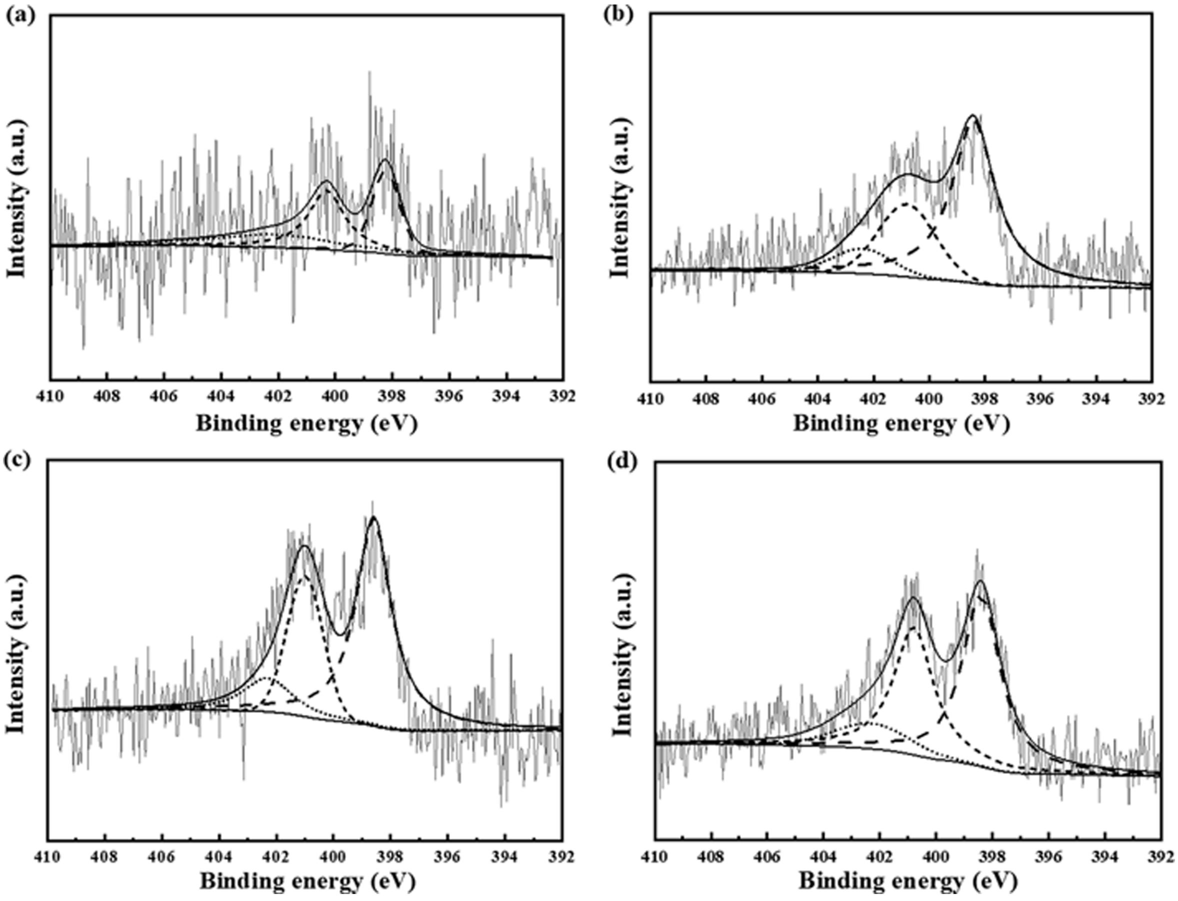

Fig. 4. N1s photoelectron peaks of (a) BM0-Fe-VGCNF, (b) BM2-Fe-VGCNF, (c) BM4-Fe-VGCNF, (d) BM6-Fe-VGCNF catalysts.

ples reveal peaks for the N1s photoelectron. The intensity of this peak varies with the ball-milling time. Compared with the peak intensity in the spectra of BM*x*-Fe-VGCNF (*x*=2, 4, 6), the intensity in the spectrum of BM0-Fe-VGCNF is low, indicating relatively low nitrogen content in BM0-Fe-VGCNF. This result is consistent with the results of elemental analysis (Table 2).

For a more precise analysis of the electronic state, the N1s photoelectron peaks were deconvoluted into three electronic states: pyridinic, pyrollic, and quaternary nitrogen [40]. The quantitative deconvolution results are summarized in Table 2. Notably, the relative intensity of these electronic states is dependent on the ball-milling time applied to samples. Compared with BM0-Fe-VGCNF, the BM*x*-Fe-VGCNFs (*x*=2, 4, 6) exhibit higher proportions of pyridinic nitrogen, indicating that the defect carbon sites are more favorable for the formation of pyridinic nitrogen than the defect-free carbon sites. Interestingly, the relative intensity of pyridinic nitrogen is highest in BM2-Fe-VGCNF and decreases with increasing ball-milling time. Unlike quaternary nitrogen, which is located in the carbon framework, pyridinic nitrogen is usually formed on the surface of carbon. As confirmed previously, the surface area of BM*x*-VGCNF (*x*=2, 4, 6) decreases with increasing ball-milling time, indicating that the number of defect sites on the surface carbon correspondingly decreases. Therefore, we expected that the formation of pyridinic nitrogen should exhibit the same trend with respect to surface area.

2. Electrochemical Performance of BM*x*-Fe-VGCNF Catalysts

To investigate the electrochemical behavior of BM*x*-Fe-VGCNF, cyclic voltammetry was conducted in N_2-saturated $HClO_4$ solution. As shown in Fig. 5(a), the cyclic voltammograms of all of the BM*x*-Fe-VGCNF examples exhibit similar shapes, where small characteristic peaks are observed for the Fe^{3+}/Fe^{2+} redox couple [41]. These peaks result from iron species supported on BM*x*-VGCNF, as confirmed by XRD analysis. The capacitance varies among samples and increases in the order BM0-Fe-VGCNF<BM6-Fe-VGCNF<BM4-Fe-VGCNF<BM2-Fe-VGCNF, which is the same trend observed for the surface area of BM*x*-Fe-VGCNF. This observation is reasonable given that the capacitance largely reflects the charge stored on the surface.

Fig. 5(b) shows the polarization curves recorded with samples immersed in O_2-saturated $HClO_4$ solution. A commercial Pt/C was also tested for comparison. Compared to the BM*x*-Fe-VGCNF catalysts, Pt/C shows higher current in the potential window of 0.8-0.3 V, indicating a superior ORR performance of Pt/C. BM0-Fe-VGCNF delivers a negligible current at potentials greater than 0.3 V, indicating poor ORR performance. Compared with BM0-Fe-VGCNF, the BM*x*-Fe-VGCNFs (*x*=2, 4, 6) exhibit better ORR performances, although their individual performances differ from each other. Among the BM*x*-Fe-VGCNFs examined, BM2-Fe-VGCNF exhibits the best catalytic performance. The kinetic current was calculated using the following equation: kinetic current

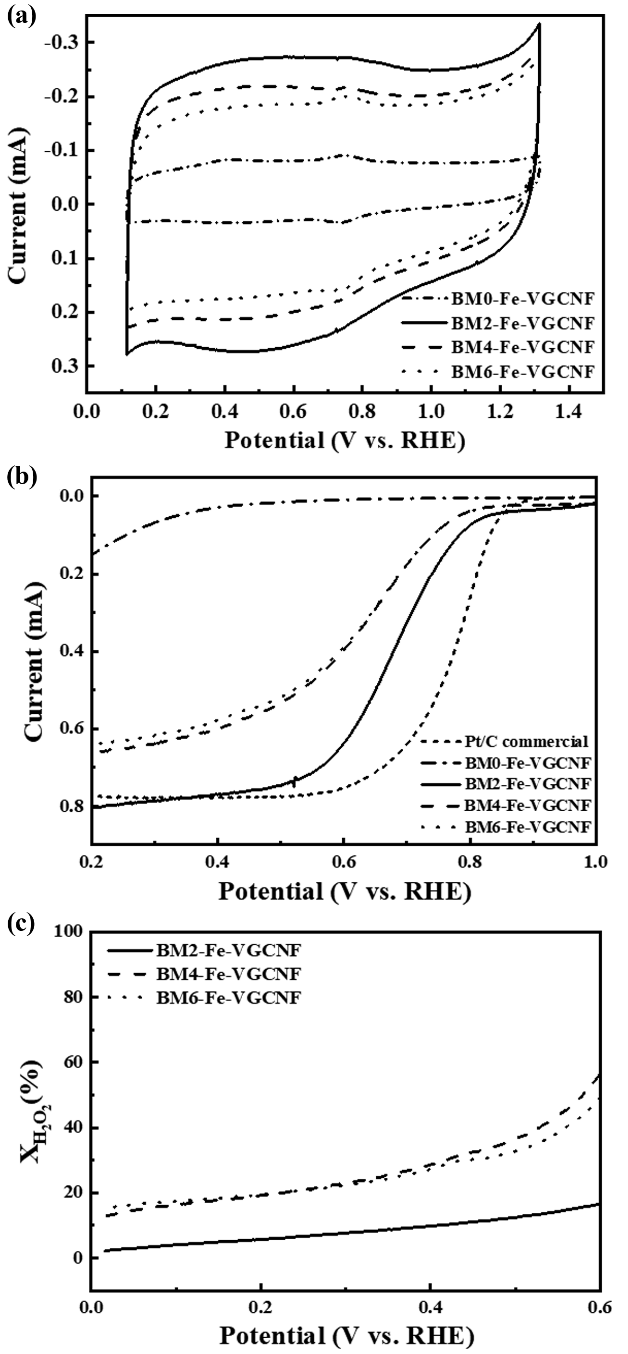

Fig. 5. (a) CVs of BM*x*-Fe-VGCNF catalysts in N_2 purged 0.1 M $HClO_4$ solution, (b) LSVs of BM*x*-Fe-VGCNF and Pt/C catalysts measured in O_2-saturated 0.1 M $HClO_4$ and the loading amount of Pt on the glassy carbon was 8 $\mu g_{Pt}/cm^2$, (c) fraction of peroxide formation of BM*x*-Fe-VGCNF catalysts.

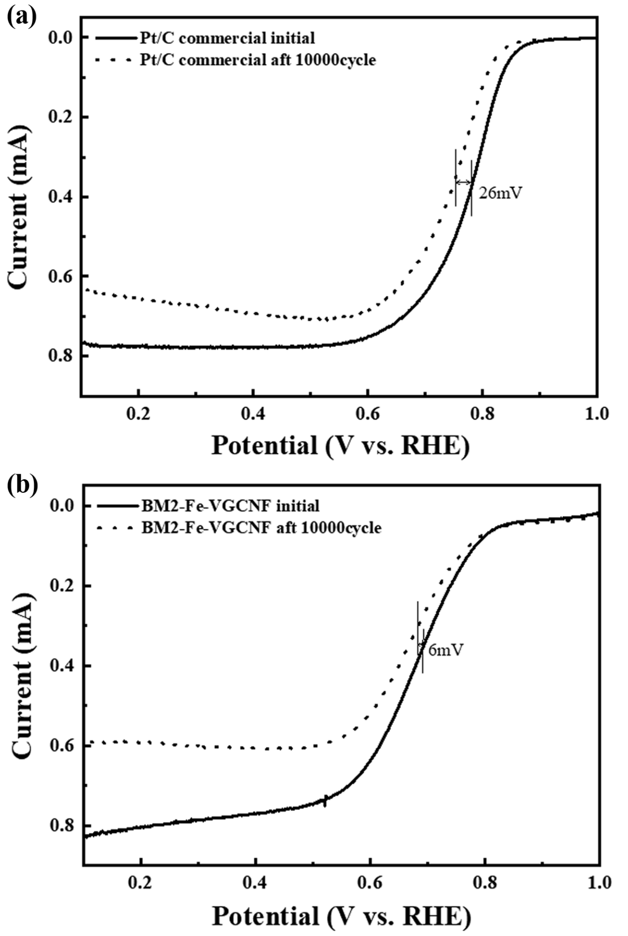

Fig. 6. LSVs before and after ADT over (a) Pt/C commercial and (b) BM*x*-Fe-VGCNF catalysts.

(i_k)=(limiting current (i_L)×measured current (i))/(limiting current (i_L)−measured current (i)), which is 0.00, 0.099, 0.040, 0.041, 0.394 mA at 0.8 V (vs. RHE) for BM0-Fe-VGCNF, BM2-Fe-VGCNF, BM4-Fe-VGCNF, BM6-Fe-VGCNF and Pt/C commercial catalyst, respectively. The kinetic current over BM2-Fe-VGCNF at 0.8 V (vs. RHE) is 2.5-times higher than that over BM*x*-Fe-VGCNFs (*x*=4, 6). The difference in the kinetic current between BM4-Fe-VGCNF and BM6-Fe-VGCNF is negligible. The superior ORR performance of BM2-Fe-VGCNF is also evidenced by the fraction of peroxide formation (Fig. 5(c)). For BM2-Fe-VGCNF, the peroxide fraction value is less than 10% (number of electrons transferred during ORR is 3.96), whereas it is greater than 55% for BM*x*-Fe-VGCNF (*x*=4, 6).

Several factors influence the ORR performance of BM*x*-Fe-VGCNF, including the type of iron species, nitrogen content, and the type of nitrogen. As confirmed by XRD analysis, all of the BM*x*-Fe-VGCNFs except BM0-Fe-VGCNF have identical iron species such as Fe_3C. Because Fe_3C exhibits ORR activity, the type of iron species should not be a decisive factor influencing the observed ORR performance [29,42-44].

Nitrogen content is also important factor affecting the catalytic performance. However, the nitrogen content in BM2-Fe-VGCNF is lower than that in BM4-Fe-VGCNF and BM6-Fe-VGCNF, even though the former catalyst delivers greater kinetic current than the latter catalysts. Therefore, the nitrogen concentration is not the sole factor determining the ORR performance of the samples. Rather, a combined effect of nitrogen content and the electronic state of nitrogen is the dominant factor governing ORR performance, because the catalytic activity is dependent on the nitrogen type. Among the investigated nitrogen types, pyridinic nitrogen is known to exhibit the greatest activity [14,45]. Although BM2-Fe-VGCNF contains less nitrogen than BM4-Fe-VGCNF and BM6-Fe-VGCNF, the difference in nitrogen content between them is small. Furthermore, pyridinic nitrogen is highest in BM2-Fe-VGCNF. These factors demonstrate that BM2-Fe-VGCNF exhibits the highest ORR activity. To evaluate the durability of catalysts, ADT was performed on Pt/C and BM2-Fe-VGCNF by potential cycling in O_2-purged 0.1 M $HClO_4$ solution. As shown in Fig. 6, both samples deliver decreased current after 10,000 potential cycle, indicating the degradation of catalytic activity. The half-wave potentials of BM2-Fe-VGCNF and Pt/C after 10,000 potential cycling decrease by 6 and 26 mV, respectively. This proves that BM2-Fe-VGCNF is more durable than Pt/C.

CONCLUSIONS

Nonprecious electrocatalysts for the ORR were prepared by NH_3 pyrolysis of Fe-ion-adsorbed VGCNF. To facilitate the formation of highly active sites, we introduced defect sites by ball-milling VGCNF. The analysis results showed that the ball-milling treatment of VGCNF was effective in generating defect sites and increasing the surface area of VGCNF. In addition, the introduction of defect sites on VGCNF was easily controlled by varying the ball-milling time. The defect sites increased with increasing ball-milling time, and BM2-VGCNF exhibited the largest surface area. The generated defect sites played a positive role in the introduction of nitrogen and, consequently, in the formation of active sites on VGCNF. For this reason, all of the catalysts (BMx-Fe-VGCNF; x=2, 4, 6) derived from the ball-milled VGCNF showed superior ORR performance compared with the catalyst prepared without ball-milling (BM0-Fe-VGCNF). In particular, BM2-Fe-VGCNF exhibited the best ORR performance even though its nitrogen content was less than that of BMx-Fe-VGCNF (x=4, 6). In addition to the nitrogen content, the electronic state of nitrogen is speculated to be another important factor determining the ORR performance of prepared catalysts. Among the catalysts studied, BM2-Fe-VGCNF exhibited the highest proportion of pyridinic nitrogen, which was responsible for its superior ORR performance.

ACKNOWLEDGEMENTS

This work was supported by the National Research Foundation of Korea (NRF) grant funded by the Korea government (MIST) (2018M1A2A2061975, 2018M1A2A2061982, 2018R1A4A1025528, 2019R1A6A3A01096629, 2019R1A2C1004151). It was also supported by Korea Basic Science Institute (KBSI), Jeonju branch. TEM samples were analyzed by Transmission Electron Microscope (JEM-2010, JEOL) installed in the Center for University-Wide Research Facilities (CURF) at Jeonbuk National University.

REFERENCES

1. K. Sopian and W. R. Wan Daud, *Renew. Energy*, **31**, 719 (2006).
2. H. Liu, C. Song, L. Zhang, J. Zhang, H. Wang and D. Wilkinson, *J. Power Sources*, **155**, 95 (2006).
3. N. M. Markovic, B. N. Grgur and P. N. Ross, *J. Phys. Chem. B*, **101**, 5405 (1997).
4. B. C. H. Steele and A. Heinzel, *Nature*, **414**, 345 (2001).
5. J. Wee, K. Lee and S. Kim, *J. Power Sources*, **165**, 667 (2007).
6. X.Yu and S. Ye, *J. Power Sources*, **172**, 145 (2007)
7. M. Lefevre, J. P. Dodelet and P. Bertrand, *J. Phys. Chem. B*, **106**, 8705 (2002).
8. A. J. Wagner, G. M. Wolfe and D. H. Fairbrother, *Appl. Surf. Sci.*, **219**, 317 (2003).
9. N. Alonso-Vante, M. Fieber-Erdmann, H. Rossner, E. Holub-Krappe, C. Giorgetti, A. Tadjeddine, E. Dartyge, A. Fontaine and R. Frahm, *J. Phys. IV*, **7**, 887 (1997).
10. P. H. Matter, L. Zhang and U. S. Ozkan, *J. Catal.*, **239**, 83 (2006).
11. W. E. Mustain and J. Prakash, *J. Power Sources*, **170**, 28 (2007).
12. P. A. Adcock, S. V. Pacheco, K. M. Norman and F. A. Uribe, *J. Electrochem. Soc.*, **152**, A459 (2005).
13. V. Tripković, F. Abild-Pedersen, F. Studt, I. Cerri, T. Nagami, T. Bligaard and J. Rossmeisl, *Chem. Cat. Chem.*, **4**, 228 (2012).
14. L. Samiee, F. Shoghi and A. Vinu, *Appl. Surf. Sci.*, **265**, 214 (2013).
15. D. J. Ham and J. S. Lee, *Energies*, **2**, 873 (2009).
16. M. Rosenbaum, F. Zhao, U. Schröder and F. Scholz, *Angew. Chem. Int. Ed.*, **45**, 6658 (2006).
17. S. Stariha, A. Serov, K. Artyushkova and P. Atanassov, *J. Electrochem. Soc.*, **37**, 1295 (2015).
18. C. Gumeci, N. Leonard, B. Halevi and S. C. Barton, *J. Electrochem. Soc.*, **26**, 1579 (2015).
19. P. Atanassov, A. Serov, K. Artyushkova and B. Kiefer, *J. Electrochem. Soc.*, **21**, 950 (2014).
20. J. Zhang and L. Dai, *ACS Catal.*, **5**, 7244 (2015).
21. D. W. Kim, O. Li and N. Saito, *Phys. Chem. Chem. Phys.*, **17**, 407 (2015).
22. H. Zhang, H. Osgood, X. Xie, Y. Shao, and G. Wu, *Nano Energy*, **31**, 331 (2017).
23. H. T. Chung, D. A. Cullen, D. Higgins, B. T. Sneed, E. F. Holby, K. L. More and P. Zelenay, *Science*, **357**, 479 (2017).
24. E. F. Holby, G. Wu, P. Zelenay and C. D. Taylor, *J. Phys. Chem. C*, **118**, 14388 (2014).
25. F. Charreteur, F. Jaouen, S. Ruggeri and J. P. Dodelet, *Electrochim. Acta*, **53**, 2925 (2008).
26. G. Ren, X. Lu, Y. Li, Y. Zhu and L. Dai, *ACS Appl. Mater. Interfaces*, **8**, 4118 (2016).
27. H. Shen, T. Thomas, S. A. Rasaki, A. Saad, C. Hu, J. Wang and M. Yang, *Electrochem. Energy Rev.*, **2**, 252 (2019).
28. Q. Wang, Z. Zhou, Y. J. Lai, Y. You, J. G. Liu, X. L. Wu and N. Tian, *J. Am. Chem. Soc.*, **136**, 10882 (2014).
29. W. Jiang, L. Gu, L. Li, Y. Zhang, X. Zhang, L. J. Zhang and L. J. Wan, *J. Am. Chem. Soc.*, **138**, 3570 (2016).
30. Z. Wu, X. Xu, B. Hu, H. W. Liang, Y. Lin, L. F. Chen and S. H. Yu, *Angew. Chem. Int. Ed.*, **54**, 8179 (2015).
31. S. Yasuda, A. Furuya, Y. Uchibori, J. Kim and K. Murakoshi, *Adv. Funct. Mater.*, **26**, 738 (2016).
32. L. Feng, N. Xie and J. Zhong, *Materials*, **7**, 3919 (2014).
33. D. Liu and Y. Long, *ACS Appl. Mater. Interfaces*, **7**, 24063 (2015).
34. B. Men, Y. Sun, J. Liu, Y. Tang, Y. Chen, P. Wan and J. Pan, *ACS Appl. Mater. Interfaces*, **8**, 19533 (2016).
35. T. Xing, L. H. Li, L. Hou, X. Hu, S. Zhou, R. Peter and Y. Chen, *Carbon*, **57**, 515 (2013).
36. F. T. Johra, J. W. Lee and W. G. Jung, *J. Ind. Eng. Chem.*, **20**, 2883

(2014).
37. X. Gao, N. Yokota, H. Oda, S. Tanaka, K. Hokamoto and P. Chen, *Crystals*, **8**, 104 (2018).
38. E. Proietti, S. Ruggeri and J. P. Dodelet, *J. Electrochem. Soc.*, **155**, B340 (2008).
39. M. Lefevre and J. P. Dodelet, *Electrochim. Acta*, **53**, 8269 (2008).
40. G. Liu, X. Li, P. Ganesan and B. N. Popov, *Appl. Catal. B*, **93**, 156 (2009).
41. G. Wu, K. L. More, C. M. Johnston and P. Zelenay, *Science*, **332**, 443 (2011).
42. Y. Hu, J. O. Jensen, W. Zhang, S. Martin, R. Chenitz, C. Pan and Q. Li, *J. Mater. Chem. Assn*, **3**, 1752 (2015).
43. W. Yang, X. Liu, X. Yue, J. Jia and S. Guo, *J. Am. Chem. Soc.*, **137**, 1436 (2015).
44. Y. Niu, X. Huang and W. Hu, *J. Power Sources*, **332**, 305 (2016).
45. K. Artyushkova, I. Matanovic, B. Halevi and P. Atanassov, *J. Phys. Chem. C*, **121**, 2836 (2017).